

Genesis of Typhoon Chanchu (2006) from a Westerly Wind Burst Associated with the MJO. Part II: Roles of Deep Convection in Tropical Transition

WALLACE HOGSETT AND DA-LIN ZHANG

Department of Atmospheric and Oceanic Science, University of Maryland, College Park, College Park, Maryland

(Manuscript received 24 March 2010, in final form 5 November 2010)

ABSTRACT

In this study, the life cycles of a series of four major mesoscale convective systems (MCSs) during genesis and their roles in transforming a vertically tilted vortex associated with a westerly wind burst (hereafter the WWB vortex) into Typhoon Chanchu (2006) are examined using 11-day cloud-resolving simulations presented in Part I. It is found that the tilted WWB vortex at early stages is characterized by an elevated cold-core layer (about 200 hPa thick) below and a weak warm column above with large vertical wind shear across the layer, which extends over a horizontal distance of about 450 km between the vortex's 400- and 900-hPa centers. During the final two days of the genesis process, the upper-level warm column increases in depth and intensity as a result of the absorption of convectively generated vortices (CGVs), including a mesoscale convective vortex (MCV), causing more rapid amplification of cyclonic vorticity in the middle than the lower troposphere. The commencement of sustained intensification of Chanchu occurs when the upper-level warm column is vertically aligned with the surface-based warm-core vortex.

Results show that four unique MCSs develop in succession on the downtilt-right side of the WWB vortex. The first MCS develops as a squall line with trailing stratiform precipitation and an MCV; subsequent MCSs include a convective cluster whose shape changes from an inverted U to a question mark and finally a spiral rainband as the WWB vortex decreases its vertical tilt. Strong cold pools are favored behind the leading convective lines during the earlier tilted-vortex stages due primarily to dry intrusion by the midlevel sheared flows, whereas few cold downdrafts occur at later stages as the WWB vortex becomes more upright and sufficiently moist. The authors conclude that the roles of the MCSs during genesis are to (a) generate cyclonic vorticity and then store it mostly in the midtroposphere, after merging CGVs within the WWB vortex; (b) moisten the low- and midlevels; (c) enhance the northward displacement of the WWB vortex; and (d) reduce the vertical tilt of the WWB vortex.

1. Introduction

Tropical cyclogenesis (TCG) remains an enigmatic phenomenon because many of the processes that precede genesis are not well observed at the mesoscale ($\sim 10^2$ km). While the preconditions for TCG are well established (e.g., Gray 1998) and persist year-round in the western North Pacific (WNP), the organization of deep convection that precedes and facilitates TCG is not yet well understood. However, as our ability to observe the tropical atmosphere has improved over the years, much progress has been made toward the understanding of TCG at smaller scales.

Recent observational and modeling studies view TCG as a stochastic phenomenon (Simpson et al. 1997) involving various mesoscale interactions that lead to the upscale growth of cyclonic vorticity and eventually result in a self-sustaining surface cyclonic circulation. Ritchie and Holland (1999) found that almost all TCG cases in the western North Pacific develop in association with at least one mesoscale convective system (MCS), which often spawn mesoscale convective vortices (MCVs) (Zhang and Fritsch 1987; Bartels and Maddox 1991; Fritsch et al. 1994; Harr and Elsberry 1996). MCVs often persist in the midlevels after their parent MCSs decay, and several studies have identified MCVs (Harr et al. 1996; Zhang and Bao 1996b) and merging vortices (Simpson et al. 1997; Ritchie and Holland 1997; Kieu and Zhang 2008) as precursors to TCG. As individual MCVs develop within close proximity, they may interact and merge into a larger and stronger MCV, particularly

Corresponding author address: Dr. Da-Lin Zhang, Department of Atmospheric and Oceanic Science, University of Maryland, College Park, College Park, MD 20742–2425.
E-mail: dalin@atmos.umd.edu

if several small MCVs exist within a larger cyclonic circulation, such as the western Pacific monsoon trough (Simpson et al. 1997). The phenomenon of vortex mergers is widely believed to play an important role in some TCG cases, and Houze (2004) suggested that MCVs are the building blocks of tropical cyclones (TCs). Recently, Kieu and Zhang (2008) found that the genesis of Tropical Storm Eugene (2005) resulted from the merging of two mesovortices, spawned from MCSs within the intertropical convergence zone (ITCZ). Obviously, the result of merging vortices is the formation of a larger and stronger vortex. But for a sustained TCG process to take place, cyclonic circulation must increase near the surface.

There has been considerable discussion on the amplification of near-surface vorticity during TCG—that is, through the so-called top-down (Bister and Emanuel 1997) and bottom-up pathways (Zhang and Bao 1996a,b; Hendricks et al. 2004; Montgomery et al. 2006)—in reference to the vertical direction of vorticity growth. However, still uncertain are the roles of convectively generated vortices (CGVs) of different scales—that is, from MCVs to vortical hot towers (VHTs; see Hendricks et al. 2004)—in determining TCG. In particular, little work has been done to differentiate the lower-level from midlevel vorticity growth during the *genesis* stage. To facilitate our subsequent discussion, we define herein the genesis as a stage of slow evolution with few or fluctuating intensity changes, even after tropical depression (TD) formation, which is followed by a period of sustained intensification (SI) at a rate of at least 8 hPa day^{-1} for longer than 12 h. The term TCG is loosely used herein to represent processes occurring during both stages. Note that this definition differs from that used in some of the previous studies in that the onset of sustained pressure deepening marks the end of genesis.¹

It appears that previous observational studies of genesis have focused more on the development of MCSs than the resulting midlevel cyclonic vorticity in relation to the TD-scale circulations. For example, Zipser and Gautier (1978, hereafter ZG78) analyzed the largest MCS during the Global Atmospheric Research Program (GARP) Atlantic Tropical Experiment (GATE) that occurred within a slowly intensifying TD. ZG78 found that as the MCSs cloud shield evolved from circular in shape to more comma-shaped with time, the midlevel circulation center occurred westward of that at the low levels (see Figs. 6 and 7 therein). Despite the large size of the MCS, ZG78 detected no low equivalent potential temperature (θ_e) moist downdrafts. The three-dimensional (3D)

structures and evolution of the storm-scale vorticity in their case was unknown because of the lack of high-resolution observations over the tropical ocean.

In Part I of this series of papers (i.e., Hogsett and Zhang 2010, hereafter Part I) we presented an 11-day (i.e., 0000 UTC 27 April–0000 UTC 8 May 2006) cloud-resolving simulation of the genesis of Typhoon Chanchu (2006) that occurred in the near-equatorial western Pacific during the active phase of the Madden–Julian oscillation (MJO) using the quadruply nested (54/18/6/2 km) version of the Weather Research and Forecast (WRF) model. The simulation begins with a low-level trough near the equator to the north of a synoptic-scale westerly wind burst (WWB) associated with the MJO at 0000 UTC 27 April (hereafter 27/00–00). The simulated incipient disturbance evolves to a closed circulation (i.e., TD) by 30/00–72 (i.e., 72 h into the simulation), and begins SI at 5/00–192. Results show that the WWB, under the influence of a convectively coupled Kelvin wave, accounts for the generation of a synoptic westward-tilted vortex with organized cyclonic rotation up to 400 hPa, hereafter referred to as the WWB vortex. The presence of large vertical wind shear (VWS) across the vortex layer and higher θ_e air in the low-level easterly flow, together with equatorial wave dynamics, gives rise to the development of deep convection at a preferred location (i.e., on the downtilt-right side; see section 5b in Part I). The genesis period is characterized by an increasingly upright vortex that deflects northward off of the equator mainly as a result of persistent convective overturning on the downtilt-right side. Although the simulated SI begins 2 days prior to that observed, it occurs within 200 km of the location of the observed (see Fig. 7 in Part I). It should be mentioned that the WWB vortex could also form from the incipient trough, with its vertical tilt progressively decreased in a dry simulation (hereafter DRY) in which diabatic heating is turned off while holding all the other parameters identical to the control run (hereafter CTL) presented in Part I.

The objectives of the present study are to (i) examine the 3D structures and evolution of a series of MCSs and an MCV in relation to the tilted WWB vortex during the genesis stage; (ii) clarify the impact of CGVs on the transition of the synoptic tilted vortex to Typhoon Chanchu and the roles of the MCSs prior to SI; and (iii) gain insight into the trigger of SI as the tilted WWB vortex is transformed to an upright orientation. The objectives will be achieved using cloud-resolving simulations of the case mostly from the 6-km resolution domain, unless otherwise mentioned. It should be emphasized that although we wish to explore the genesis of the real Chanchu, we investigate only the model-simulated fields herein, and differences in the structures and evolution

¹ By the definition established herein, operational centers will issue advisories during our genesis stage.

between the simulated and observed storms certainly exist, particularly at the convective scale.

The next section shows the distribution of larger-scale flows and precipitation with respect to the vertically tilted WWB vortex during the genesis and SI stages in order to provide a general framework for the subsequent discussion of tropical transition processes. Section 3 describes the 3D structures and evolution of four MCSs and a shallow arc-shaped rainband in relation to the tilted WWB vortex, as well as their contributions to the system-scale vorticity during genesis. Section 4 presents the transition of the WWB vortex from a weak baroclinic system to a warm-cored TC and discusses the trigger of SI. A summary and concluding remarks are given in the final section.

2. An overview of genesis

Figure 1 provides an overview of the low- and midlevel evolution of the horizontal flows and relative vorticity as well as the simulated radar reflectivity during the final two days of genesis and the early SI stage of Chanchu. At 3/00–144 (i.e., 48 h prior to SI; see Figs. 1a,e), the vertically tilted WWB vortex circulations occur at scales of more than 1000 km, with the 600-hPa center (A) located about 450 km to the west-northwest of the 900-hPa center (C); this horizontal distance between A and C represents the degree of vertical tilt of the WWB vortex between 600 and 900 hPa. A north–south-oriented convective rainband, as defined by a large gradient of radar reflectivity, develops to the north of C on the downtilt-right side of the tilted WWB vortex, which is a favorable location for isentropic lifting of the moist maritime boundary layer (MBL) air, as mentioned in section 1. The mid- and upper-level easterly flows account for the generation of extensive trailing stratiform clouds to the north and west of the convection (Fig. 1e). A cyclonic vorticity (ζ^+) band (V; Fig. 1a) will be shown in section 3 as an MCV that develops behind the leading rainband. The associated cyclonic vorticity generated by precipitation processes serves to generate a deep midlevel trough, with another vorticity center situated in the trailing stratiform region (Fig. 1a).

Of importance is that A and V are embedded within a midlevel large cyclonic envelope modulated by the WWB, which is a favorable configuration for merger (Simpson et al. 1997). Indeed, A and V begin to merge by 4/00–168 (Fig. 1b). Of interest is that unlike the vortex merger in Kieu and Zhang (2008), the present merging process is confined to the midlevels and does not cause significant changes in the surface flow fields (see Fig. 2a). The resulting vortex (AV) contracts and exhibits a more circular shape with the peak ζ^+ of greater than $2 \times 10^{-4} \text{ s}^{-1}$ near the vortex center at 5/00–192 (Fig. 1c).

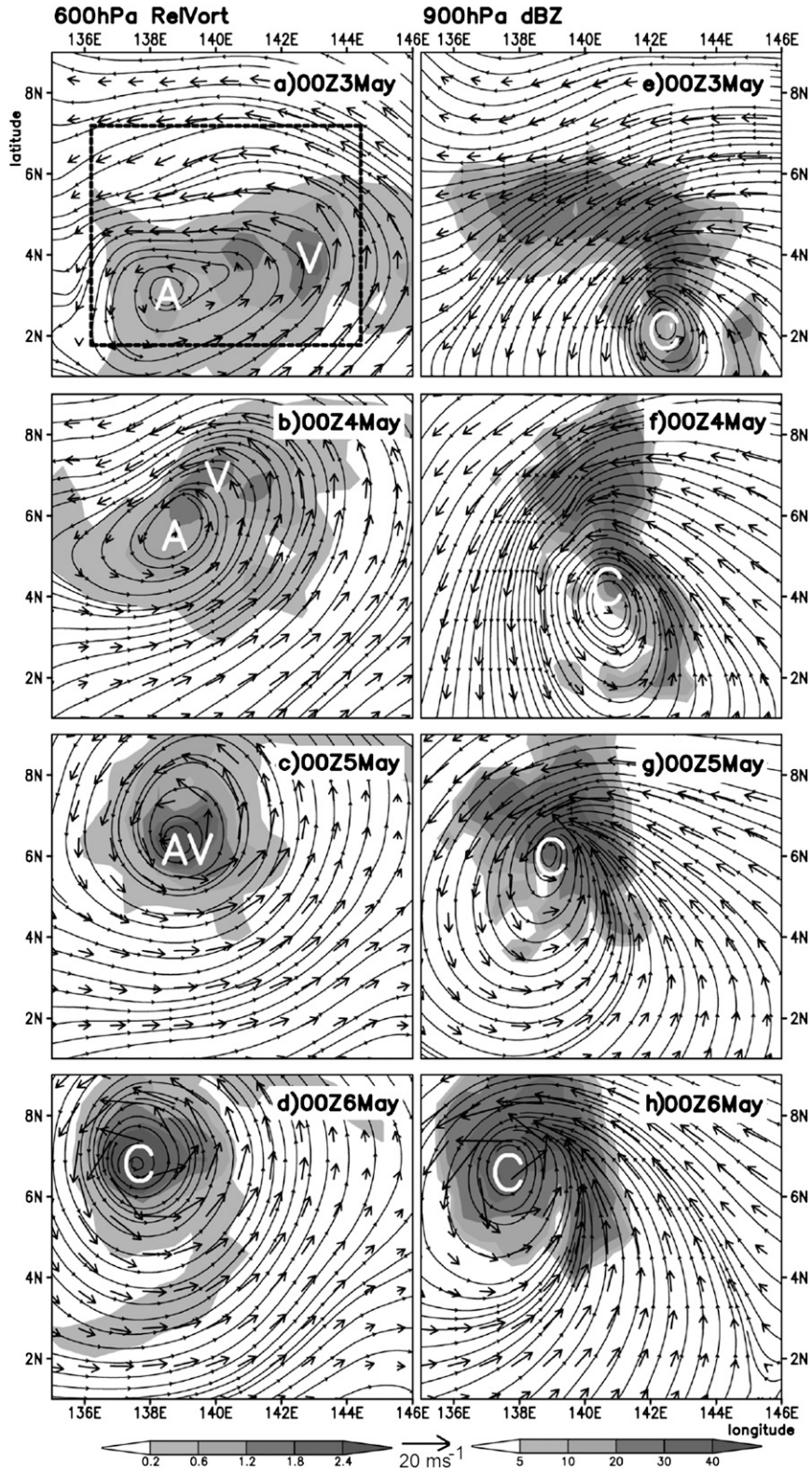
Meanwhile, the centers of AV and C become nearly collocated, signifying the SI of Chanchu with a comma-shaped rainband in its inner-core region.

The time series of the maximum surface wind V_{\max} and the minimum sea level central pressure P_{\min} at high temporal resolution, given in Fig. 2a, shows that a TD, which is the precursor of Chanchu, reaches tropical storm (TS) intensity (i.e., $>17.5 \text{ m s}^{-1}$) even at 3/00–144. Despite its localized high V_{\max} , P_{\min} remains above 1000 hPa and fluctuates significantly with roughly a daily cycle. In particular, P_{\min} does not begin to deepen continuously for a period of 12 h until 5/00–192. Based on our definition, this time may be used to demarcate the genesis and SI stages. As will be discussed in section 4, it is important to distinguish the genesis and SI periods based on surface pressure falls and not simply surface wind speed.²

While the magnitude of V_{\max} exceeds the threshold for a TS throughout genesis, the location (not shown) of V_{\max} during 3–5 May appears to be closely associated with the distribution of four MCSs, hereafter referred to as MCS1–4 (their durations are marked in Fig. 2a), that develop to the north of C. They are distinct in structure and intensity from a weak and shallow, arc-shaped rainband that wraps around the eastern semicircle of C (Figs. 1f,g). Of interest is that the life cycles of the four MCSs coincide well with the fluctuation of P_{\min} but have little long-lasting impact on P_{\min} or V_{\max} , as SI does not begin until near the end of MCS4.

Of particular relevance to the present study is that the midlevel cyclonic vorticity $\bar{\zeta}_{600}$ begins to increase at 3/00–144 (Fig. 2b), accelerates shortly after 4/00–168, and more than doubles in magnitude between 3/00–144 and 5/00–192. On the other hand, the low-level relative vorticity $\bar{\zeta}_{900}$ increases by only 20% during the same period. Note that $\bar{\zeta}_{900}$ commences its slow amplification after the arc-shaped rainband around C increases its intensity and coverage (cf. Figs. 2b and 1f). Similarly, only small changes in the mean surface wind speed V_{mean} and the mean surface heat fluxes (HFX) occur during the genesis stage in spite of continued MCS development (Fig. 2a). Note that all the vortex-scale variables presented herein are calculated by using an area of $400 \text{ km} \times 400 \text{ km}$ following C, except for $\bar{\zeta}_{600}$, which is calculated following A (and AV postmerger). In addition, we define the system scale as the $(600 \text{ km} \times 600 \text{ km})$ area average centered between A and C including the rainband(s) to the north. The different behaviors between the low- and midlevel rotational development and their relation to the

² The magnitudes of V_{\max} (P_{\min}) shown in Fig. 2 are greater (smaller) than those given in Fig. 8 of Part I because of the use herein of higher (6 vs 18 km) resolution data.



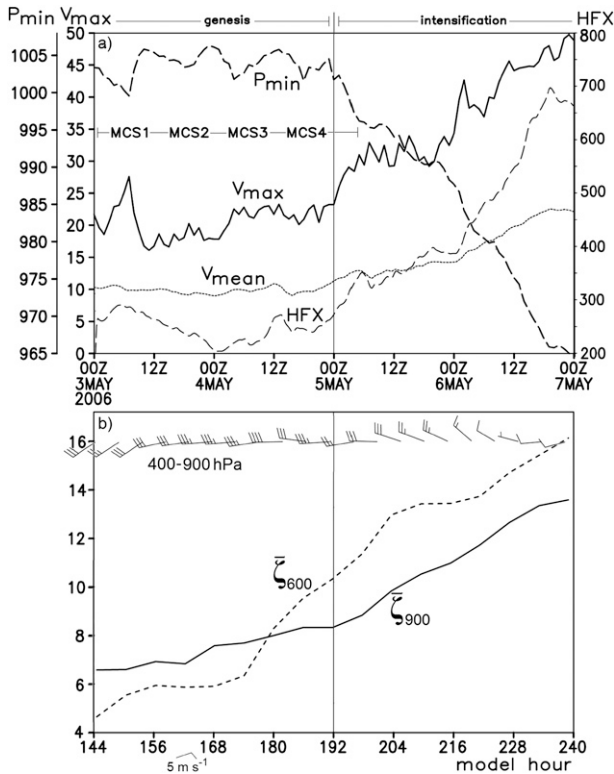


FIG. 2. (a) Time series (at 60-min intervals) of P_{min} (hPa), V_{max} ($m s^{-1}$), and the area-averaged ($400 km \times 400 km$) HFX ($W m^{-2}$, dashed) and V_{mean} ($m s^{-1}$) during the 4-day ($\Delta x = 6 km$) simulation (i.e., from 3/00–144 to 7/00–240), which follows the circulation center C. (b) As in (a), but for $\bar{\zeta}_{600}$ ($10^{-5} s^{-1}$) centered at A and $\bar{\zeta}_{900}$ centered at C, and the area-averaged vertical shear (full barb is $5 m s^{-1}$) between 900 and 400 hPa centered at C. The thin vertical line at 0000 UTC 5 May demarcates the genesis and sustained intensification periods.

series of four MCSs will be the subjects of the next two sections.

The simulated Chanchu begins SI at 5/00–192, as shown by continuous increases in V_{max} , V_{mean} , HFX, $\bar{\zeta}_{900}$, $\bar{\zeta}_{600}$, and the continuous drop in P_{min} , when the midlevel vortex AV aligns vertically with C (cf. Figs. 1c,g and 2a,b). Note that the present SI occurs after more than 5 days of intensity fluctuations at the TS stage,

during which period the surface circulation with $V_{max} > 17.5 m s^{-1}$ is a persistent feature. Apparently, such a long time scale for the onset of SI is attributable to the vertical tilt of the WWB vortex, despite the obvious organization of deep convection and increase in the midlevel rotation through the convective enhancement and vortex-merging processes (Figs. 1a and 2b). Nevertheless, even though the circulation centers become coherent in the vertical at the onset of SI, the VWS between 900 and 400 hPa in the near-storm environment remains significant (i.e., $>15 m s^{-1}$; see Fig. 2b), although the synoptic-scale VWS is only $5-8 m s^{-1}$ (see Fig. 8 in Part I). It should be mentioned that the 900–400-hPa (rather than the typical 850–200 hPa) layer VWS is utilized herein because this is the layer in which the tilted WWB vortex is embedded (Figs. 3b and 4b).

While the MJO (and a convectively coupled Kelvin wave) accounts for the formation of the WWB vortex, as detailed in Part I, it appears to be the CGVs and their merging into the WWB vortex (e.g., the A–V merger) that play important roles in the intensification of the midlevel rotational flows. When the WWB vortex becomes upright, surface intensification continues as long as deep convection could persist in the inner-core regions. In Part I, we have shown an example of aborted intensification beginning near 2/00–120, at which time an upright vortex forms as a result of the interaction between CGVs and the WWB vortex. However, SI is aborted shortly after deep convection weakens, and subsequently the WWB vortex tilts westward again under the influence of easterly VWS. Thus, our discussion of genesis that follows will involve mesoscale events after the simulated aborted intensification (i.e., beginning at 3/00–144) and prior to the beginning of SI at 5/00–192.

3. Development of four MCSs and their vortical contributions

In this section, we focus on the impact of a series of four MCSs, as well as the arc-shaped shallow rainband, on facilitating the transition of a tilted to an upright vortex leading to the SI of Chanchu. Their general



FIG. 1. Horizontal distribution of (a)–(d) the 600-hPa flow vectors and streamlines as well as the (700–500 hPa) layer-averaged relative vorticity (shaded, $10^{-4} s^{-1}$) and (e)–(h) the 900-hPa flow vectors and streamlines as well as radar reflectivity (shaded, dBZ), given at 24-h intervals, from the 6–9-day simulations, valid between 0000 UTC 3 May and 0000 UTC 6 May 2006, over the 54-km resolution domain. Here and in the other figures A, C, V, and AV denote respectively the location of the peak relative vorticity associated with the pre-Chanchu vortex at 600 and 900 hPa, an MCV, and the merger of A and V. The dashed box in (a) denotes the area of focus for Fig. 3.

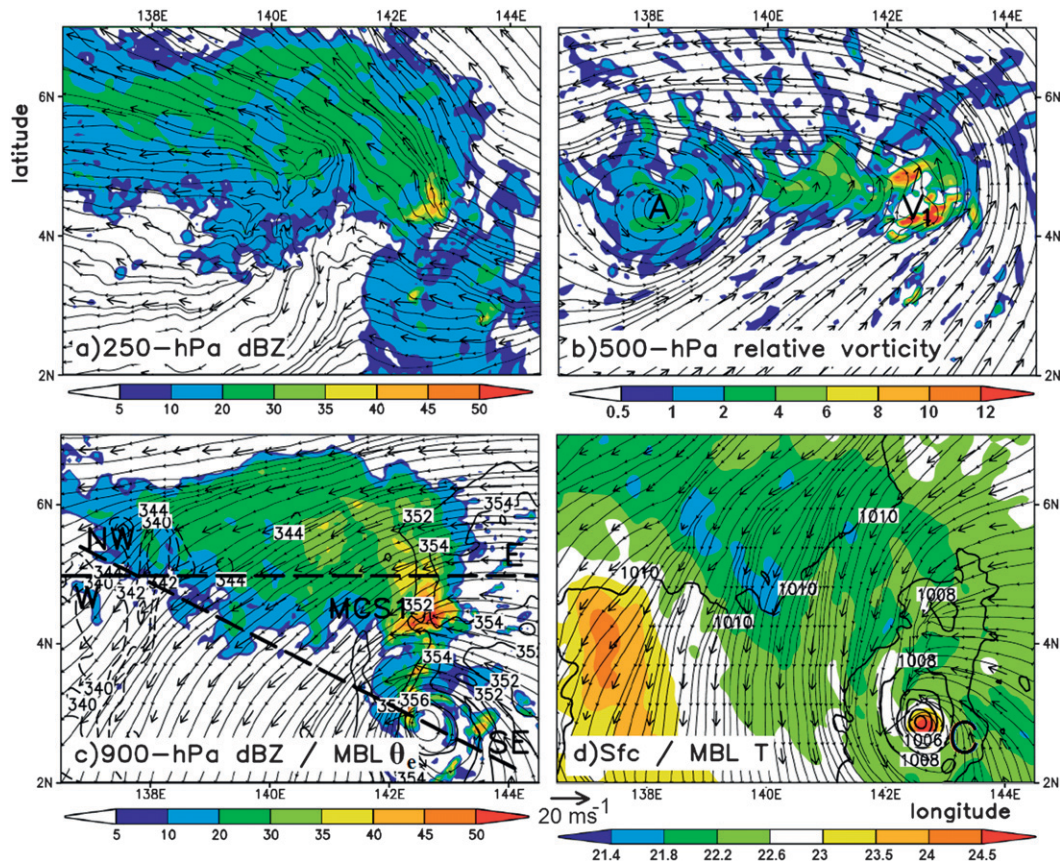


FIG. 3. Horizontal distribution of (a) the 250-hPa radar reflectivity (shaded, dBZ); (b) the 500-hPa relative vorticity (shaded, 10^{-4} s^{-1}); (c) the 900-hPa radar reflectivity (shaded, dBZ) and the surface–900-hPa layer-averaged equivalent potential temperature (contoured at 340, 342, 344, 352, 354, and 356 K); and (d) the surface–900-hPa layer-averaged temperature (shaded, $^{\circ}\text{C}$) and the sea level pressure (contoured at 1-hPa interval), superposed with the horizontal flow vectors and streamlines at the individual levels, that are taken at 3/00–144 from the 6-km resolution domain. In (b) V_1 denotes a convectively generated vorticity center (see text). The thick dashed lines W–E and NW–SE in (c) denote the locations of the vertical cross sections used in Fig. 4.

precipitation structures and associated generation of cyclonic vorticity, including the formation of the above-mentioned MCV, will also be examined.

a. Mesoscale flow structures at an early genesis stage

At 3/00–144, the near-surface disturbance exhibits a closed circulation with $P_{\min} \sim 1004 \text{ hPa}$ near 3°N (Fig. 3d). An elongated, north–south-oriented flow (and moisture) convergence line, as indicated by intersecting streamlines, appears in the MBL to the north of C (i.e., on the downtilt right side). Surface convergence is associated with a squall line, referred to as MCS1, which corresponds to the early development of the abovementioned leading rainband with strong radar reflectivity (cf. Figs. 3c,d and 1e). To the west of the leading convective line is an extensive area of trailing stratiform precipitation due to the presence of the pronounced easterly flows in the mid- to upper levels (Figs. 3a–c).

A west–east vertical cross section, taken through MCS1 (Fig. 4a), shows a vertical mesoscale flow pattern that is similar to that shown by Gamache and Houze (1982) for a typical tropical squall line. Features of interest include the lifting of high- θ_e air in the MBL easterly flow, strong ascent in the leading convective line, weak ascent (descent) above (below) the melting level in the trailing stratiform region, and a deep layer of front-to-rear (FTR) moist inflows. This easterly flow pattern in the mid- and upper levels acts to continually generate precipitation particles to maintain the large stratiform region, covering an area of nearly $80\,000 \text{ km}^2$ (Fig. 3c), which is about twice of the maximum size documented by Yuter and Houze (1998) in a study of WNP MCSs.

It is evident from Figs. 3b and 4b that MCS1 produces a deep layer of strong cyclonic vorticity (e.g., $\zeta^+ \sim 12 \times 10^{-4} \text{ s}^{-1}$ at 500 hPa) along the leading line and weaker vorticity (e.g., $\zeta^+ \sim 2 \times 10^{-4} \text{ s}^{-1}$ at 500 hPa) in the

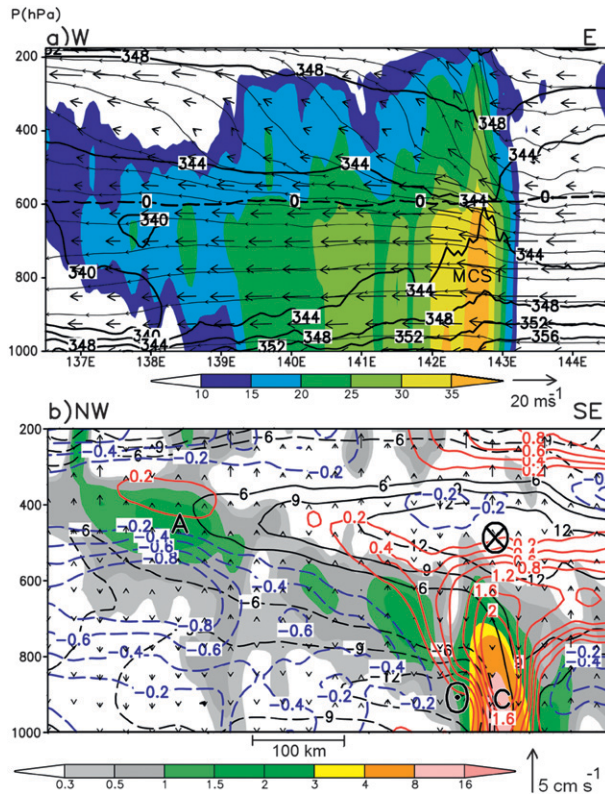


FIG. 4. (a) West-east vertical cross section of radar reflectivity (shaded, dBZ), θ_e (thick solid contours with 4-K interval), superimposed with the melting level (thick dashed line), and in-plane flow vectors and streamlines (vertical motion multiplied by a factor of 10). (b) Northwest-southeast vertical cross section of the relative vorticity (shaded, 10^{-4} s^{-1}), the cross-plane wind speed (contoured at $\pm 3, 6, 9, 12, \text{ and } 15 \text{ m s}^{-1}$) into (out of) the vertical plane with their maximum magnitude marked by a cross (dot), superimposed with deviation temperatures (thick contoured at $\pm 0.2, 0.4, 0.6, 0.8, 1.2, 1.6, \text{ and } 2.0 \text{ }^\circ\text{C}$) and vertical motion vectors. They are taken at 3/00–144 along lines given in Fig. 3c. Note that all the fields have been averaged laterally within 54 km in (a) and during a 3-h period in (b) to capture representative structures of (a) MCS1 and (b) the tilted WWB vortex, respectively.

stratiform region, which are superimposed with a broad but shallow cyclonic circulation ($\zeta^+ \sim 0.5 \times 10^{-4} \text{ s}^{-1}$) associated with the WWB vortex tilting northwestward from its 800-hPa location C to the back edge of the stratiform region at 400 hPa. The tilted vortex is only roughly 150–200 hPa deep, as defined by $\zeta^+ \sim 0.5 \times 10^{-4} \text{ s}^{-1}$ (Fig. 4b), with little cyclonic vorticity above or below the layer.

Of importance is that the tilted WWB vortex has a cold-core³ baroclinic structure with large VWS and

a weak warm layer above A, as compared to the warm-cored low-level circulation C with nearly upright isotachs in the lowest 300 hPa (Fig. 4b). Because of the tilted vortex circulations, horizontal flows change direction with height in the area overlapped by intersecting cyclonic streamlines centered between A and C. As a result, there is intense (directional) VWS (e.g., as large as 15–25 m s^{-1}) across the vortex layer, especially near the tilted radii of the maximum wind (RMWs) where the cyclonic flows are opposite in direction to those in the layers above. Such large VWS tends to inhibit deep convective development in the zone between A and C, as can be seen from Fig. 5. Furthermore, the midlevel cyclonic flows tend to transport lower- θ_e air into the convective region, thereby inducing moist downdrafts in convective regions to the north of C. As will be seen in the next four subsections, the horizontal distance between A and C and the orientation of the tilted vortex with respect to the MBL easterly flows play an important role, through VWS, moist downdrafts, and CGVs, in determining the shape and life cycle of each MCS under study.

One may note that the vertical cross-plane flow structures (i.e., the near-northerly flow below and a near-southerly flow above the vortex layer) resemble those associated with a midlatitude cold front, with the vortex layer corresponding to the “frontal zone.” A thermal gradient of $2.8 \text{ }^\circ\text{C (300 km)}^{-1}$ between the cold and warm cores corresponds qualitatively well to the large VWS in the vortex layer. This thermal gradient is weaker than that in cold-cored systems that developed into TCs at higher latitudes (e.g., Bracken and Bosart 2000; Davis and Bosart 2003).

Note that the tilted vortex axis at 3/00–144 is located along the southern edge of the cloud/precipitation regions at individual levels, except near the western edge (cf. Figs. 3c and 4b), confirming again the favorable location of the northern semicircle (i.e., downtilt-right) for convective development. In particular, the northern semicircle provides both the necessary background vorticity for vortex stretching associated with deep convection near the equator, as well as isentropic ascent to trigger convection (see section 5b in Part I). In fact, the cyclonic vorticity along the leading line of MCS1 is much stronger than that associated with the WWB vortex, and it induces a deep trough that is superimposed with the broad closed circulation in the midlevels (Fig. 3b). Twenty hours later, this trough becomes a closed MCV at 600 hPa (see Figs. 5a–f). As will be seen in the next section, the midlevel vortex-vortex interaction accounts for the merging of these CGVs with the WWB vortex and for the alignment of the closed cyclonic circulations in the vertical.

It should be mentioned that the horizontal flow structures shown in Fig. 3 appear similar to the intensifying TD

³ The thermal anomalies are denoted herein by deviation temperatures that are obtained by subtracting the mean temperature along individual horizontal slices of the cross section.

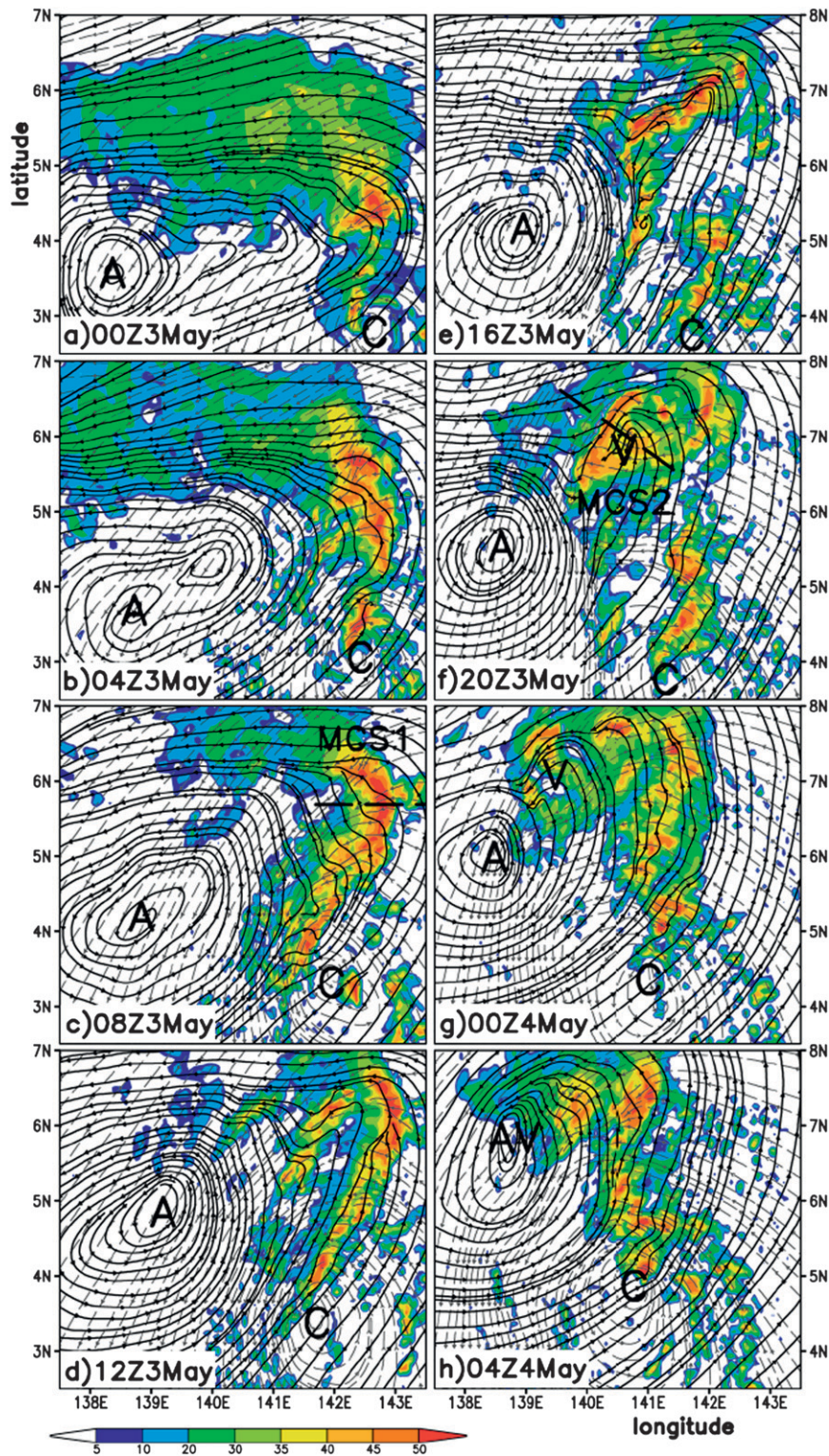


FIG. 5. Evolution of 900-hPa radar reflectivity (shaded, dBZ) at 4-h intervals between (a) 3/00–144 and (p) 5/12–204 from the 6-km resolution domain, superimposed with the 600-hPa (thick solid) and 900-hPa (thin dashed) streamlines. The paths of vertical cross sections (thick dashed) during the mature stage of MCS1 in (c), MCS2 in (f), MCS3 in (j), and MCS4 in (m) are denoted.

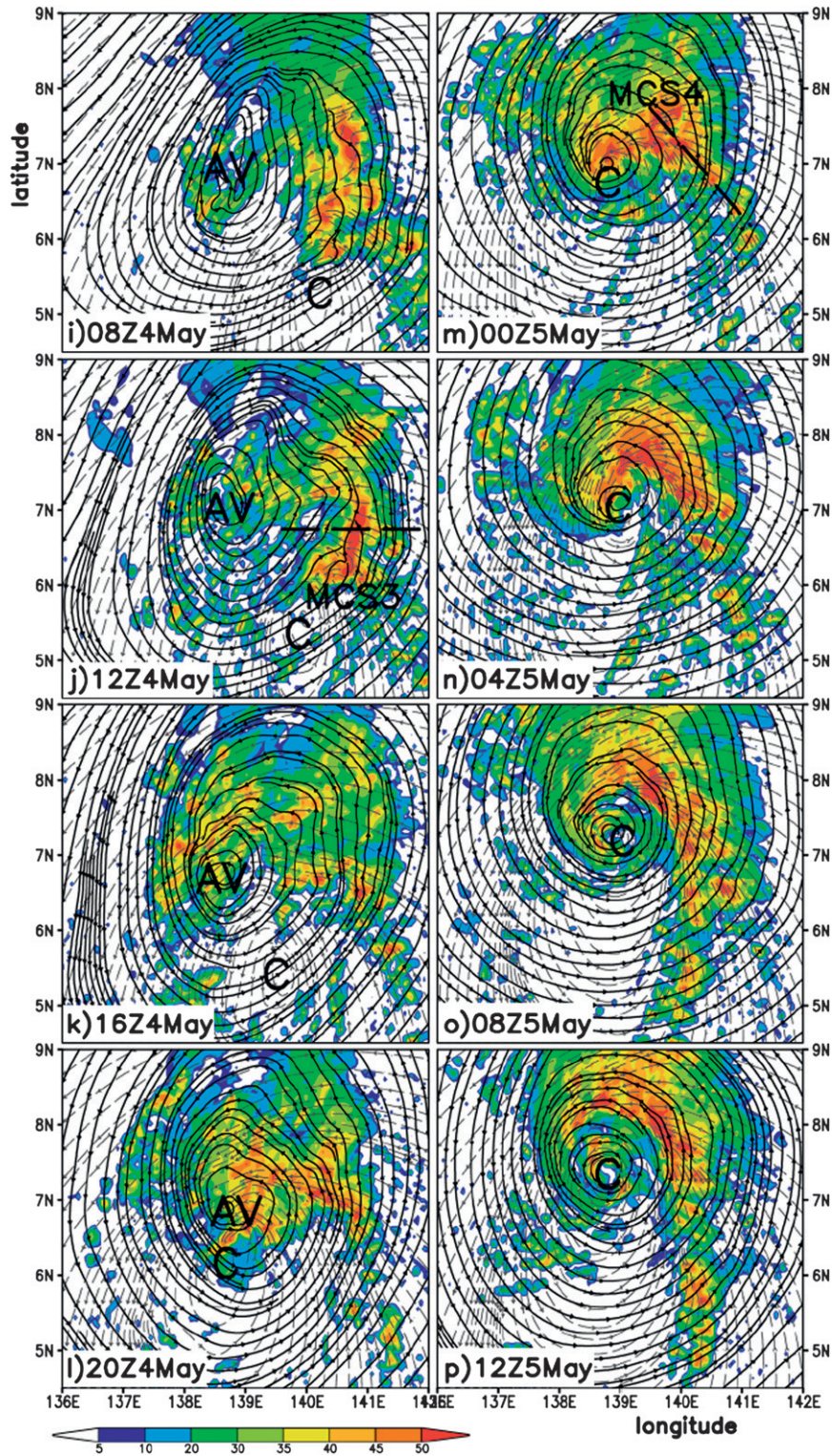


FIG. 5 (Continued)

analyzed by ZG78 in which an MCS developed in the northern semicircle and the midlevel circulation center was not only located westward of the low-level center, but also exhibited a trough that extended northeastward from the center toward the region of active convection. Data limitations prevented ZG78 from ascertaining the complete 3D structures (i.e., any tilt that may have existed) of the developing TD. Our results show clearly how the tilted vortex exhibits coherency from the surface to 400 hPa (cf. Figs. 3b,c and 4b).

While the WWB vortex core remains mostly free of precipitation, its northwestern one-third portion is situated above an area of stratiform precipitation, which is likely advected beneath the vortex layer by the northerly flow (Fig. 4b). As precipitation falls through the low- θ_e layer below (Fig. 4a), evaporation-driven (and melting-driven) moist downdrafts occur beneath the trailing stratiform region, more significantly in the region between A and MCS1 (see Fig. 3d). The downdrafts account for the generation of the lowest- θ_e air at 900 hPa, with a θ_e value (i.e., 340 K) similar to that in the 800–600-hPa layer, and a west–east θ_e gradient in the lower troposphere (cf. Figs. 3c and 4a). Because the precipitation available for evaporation in the downdrafts diminishes below 800 hPa, the forced cyclonic descent in the downtilt-left semicircle tends to occur isentropically, leading to the local warming near the surface to the south of A (Fig. 3d).

In sections 5b–e, we focus on the detailed structures and evolution of MCS1–MCS4, as well as their implications for TCG. For this purpose, we have superimposed in Fig. 5 the simulated radar reflectivity with streamlines at 900 and 600 hPa at 4-h intervals to show how deep convection evolves with respect to the tilted WWB vortex and what impact each MCS produces on the vortex. Although the precipitation structure shown in Fig. 5 indicates that the transition between the four MCSs is a continuous process, we discretize the evolution herein in accordance with the convective morphology along the leading line.

b. Life cycle of MCS1: Squall line

It is evident from Figs. 5a–d that the typical tropical squall line structures associated with MCS1 change significantly during the period from 3/00–144 to 3/12–156 as MCS1 matures. Specifically, the extraordinarily large stratiform region, as shown in Fig. 3c, shrinks with time as the midlevel elliptic circulation switches from a west–east to a southwest–northeast orientation with a growing area of flows in opposite directions to those in the layers below. Meanwhile, the northern portion of the leading line of MCS1 takes on a bow shape (Fig. 5c), similar to that commonly observed in midlatitude squall lines in the presence of the rear-to-front (RTF) flows (e.g.,

Houze et al. 1989; Zhang et al. 1989), while the southern convective segment is displaced to the western semicircle of the low-level circulation. Because of the intense VWS and other unfavorable conditions mentioned in section 1, only shallow convection could develop in the vicinity of C. Although no RTF flow is evident in the present case because of the presence of deep FTR flows, the increasing streamline curvature at the northern end of the squall line suggests the formation of an MCV that may weaken or alter the easterly FTR flows.

A vertical (normal line) cross section through the central portion of the bow-shaped leading convective line of MCS1, shown in Fig. 6a, shows a deep FTR (i.e., opposite to its easterly direction of propagation) inflow layer that decreases in magnitude up to 600 hPa, where the low-level easterly flows veer to the along-line direction with little normal-line flow above. Strong upward motion occurs in the leading line with the most intense cyclonic vorticity in the midlevel, which is consistent with the subsequent generation of an MCV (cf. Figs. 6a and 5a–f). Although the developing MCV is about 350 km northeast of the midlevel circulation center at 3/12–156 (Fig. 5d), together with the cyclonic vorticity along the leading line it represents the vortical contribution of MCS1 to the midlevel system-scale rotation (Fig. 2b), especially when all CGVs of different sizes are congregated. Clearly, only deep convection at the southern end of the squall line could possibly affect the surface P_{\min} (i.e., associated with C), but it is not effective in doing so since the convective line radiates outward in a linear mode rather than wrapping around as a spiral band. In addition, the southern semicircle of the tilted WWB vortex is characterized by descending motion, lower- θ_e air (Fig. 4a), and the large VWS over C's core region (Fig. 4b).

Figure 6a also shows that at the early stage of the MCV, weak RTF flow does occur in the 600–400-hPa layer, but with little descending motion, and it does not penetrate to the leading line as described in a typical squall system (Houze et al. 1989). The more significant RTF flows of the midlevel lower- θ_e air at this stage tend to occur in the southern segment of the squall line (Figs. 5a–c), as also indicated by a moderate cold pool to the south of 5°N (Fig. 7a).

c. Development of MCS2: A convective cluster

As the axis of the convectively generated trough to the north rotates cyclonically under the influence of the WWB vortex A, more midlevel lower- θ_e air can be transported into its core region, and it results in an intense cold pool behind the leading line with pronounced cold outflows (cf. Figs. 5c–f and 7b). As a result, by 3/16–160 (Fig. 5e), a Γ -shaped convective line develops along the outflow boundaries to the west and north where the

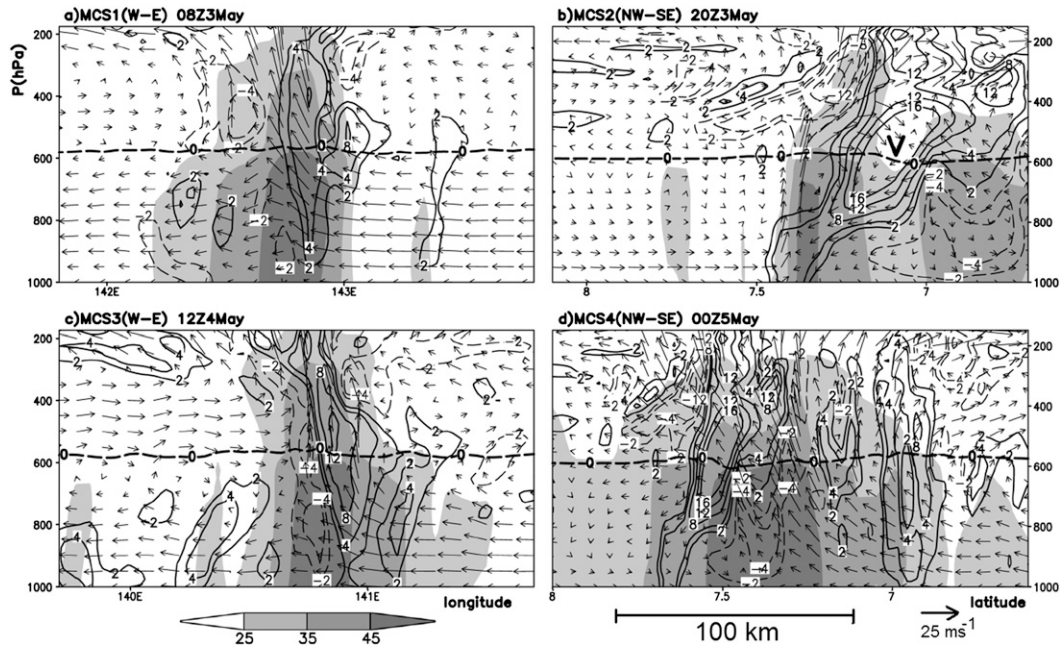


FIG. 6. Vertical cross sections of the radar reflectivity (shaded, dBZ), and relative vorticity (contoured at $\pm 2, 4, 8, 12,$ and $16 \times 10^{-4} \text{ s}^{-1}$), superimposed with in-plane flow vectors, associated with (a) MCS1, (b) MCS2, (c) MCS3, and (d) MCS4, that are taken nearly along the low-level flows given in Figs. 5c, 5f, 5j, and 5m, respectively. Vertical motion for the in-plane vectors is multiplied by a factor of 10, and thick dashed lines denote the melting level.

cold outflows converge with the north-northeasterly flows. However, the southern portion of the new convective line is short-lived because of the presence of large VWS in the overlapped region (Figs. 5d–g). As the developing MCV moves cyclonically northwestward, its wake region becomes unfavorable for deep convection, like many other observed MCSs (Biggerstaff and Houze 1991; Houze 2004), so it causes the interruption of the original leading convective line to the east (Figs. 5e,f). Thus, we may regard MCS2 as a mesoscale convective cluster, which evolves from MCS1 as a squall system (Fig. 5c) to an inverted-U-shaped MCS consisting of two convective segments (Figs. 5d–f), and a question-mark-shaped MCS as deep convection rejuvenates in the wake of the developing MCV (Fig. 5g).

Meanwhile, the weak arc-shaped rainband, which consists of scattered shallow convection east and southeast of the low-level circulation C, becomes more significant with time (cf. Figs. 5f–h). The arc-shaped rainband appears to account for the slow evolution of the low-level warm-core circulation and the amplification of ζ_{900} (and V_{\max}) after 4/00–168 (cf. Figs. 2b and 4b), as will be further shown in section 4. Apparently, the present cloud/precipitation asymmetries differ substantially from those shown in other TCG cases (e.g., Kieu and Zhang 2008; Braun et al. 2010) because of the tilted-vortex dynamics associated with the WWB vortex.

At the central portion of the question-mark-shaped convective cluster, the convectively generated mesotrough becomes almost a separate MCV entity at 3/20–164 (see V in Fig. 5f). As shown in Zhang (1992), the northern segment of a squall line favors the generation of an MCV due initially to the tilting of horizontal vorticity associated with the local large VWS, the so-called bookend vortex (Weisman and Davis 1998). MCVs such as V are a typical mesoscale phenomenon near the end of the life cycle of midlatitude MCSs (Zhang and Fritsch 1987; Menard and Fritsch 1989; Bartels and Maddox 1991), but few studies have previously examined the MCS/MCV system near the equator where the Coriolis force nearly vanishes.

The well-developed MCV, which at its mature stage has a diameter of about 50 km and a depth of 400 hPa (Fig. 6b), is initiated via tilting of horizontal vorticity (Zhang 1992) and intensified through vortex stretching associated with the strong midlevel convergence behind the leading lines of MCS1 (Fig. 8a) and MCS2 (Fig. 8b). The convergent midlevel flow and moist downdrafts below are consistent with the cold pool at the lower levels (cf. Figs. 7b and 8b). Similar to the conceptual model of Houze et al. (1989), this MCV is embedded in a region of stratiform precipitation, as evidenced by the large region of 600-hPa convergence (Fig. 8b). Of interest is that the shallow midlevel circulation A

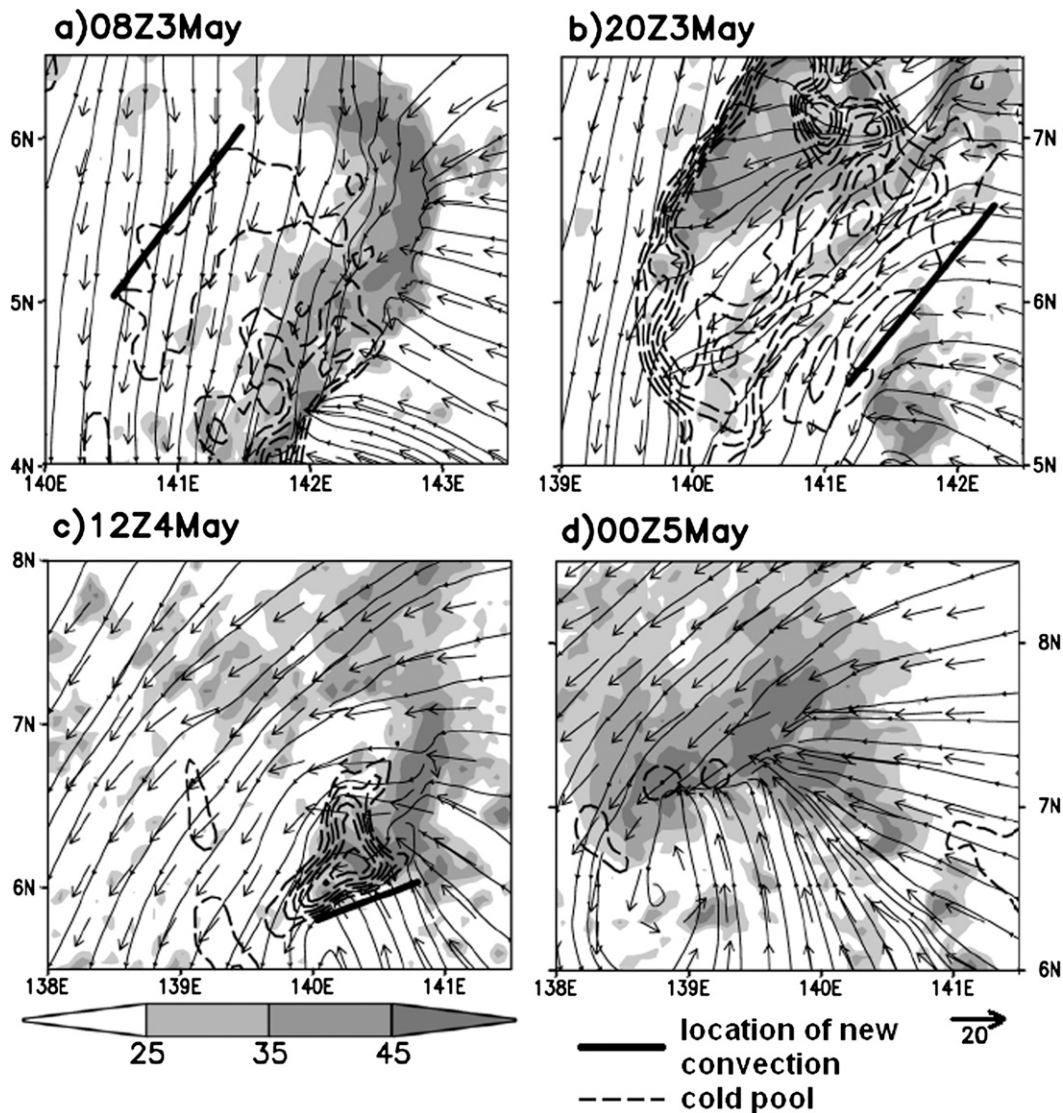


FIG. 7. Distribution of the horizontal flow vectors, streamlines, and radar reflectivity (shaded, dBZ) at 900 hPa, superimposed with the 950-hPa temperature (dashed with 0.2°C interval between 22° and 23°C) showing the cold pool associated with (a) MCS1 at 3/08–152, (b) MCS2 at 3/20–164, (c) MCS3 at 4/12–180, and (d) MCS4 at 5/00–192. Thick solid lines in (a)–(c) denote the edge of the cold pool where the subsequent MCS develops.

translates nearly 200 km northward toward the MCV during the 12-h period (cf. Figs. 5e–h) due to their mutual advection in the presence of midlevel convergence. This vortex–vortex interaction appears to account for the intensification of the midlevel system-scale cyclonic vorticity that accelerates after 4/04–172 (i.e., after the merger of A and V; cf. Figs. 2b and 5h). In this regard, we may consider the midlevel merging of MCV V (and likely other CGVs at smaller scales) with the tilted vortex as the temporal “storage” of cyclonic vorticity for the impending TCG after the cyclonic circulations at all levels become vertically coherent.

d. MCS3: Transition to a spiral rainband

After the midlevel merger of V and A (i.e., as AV), another cycle of organized convection occurs on the downtilt-right side of the WWB vortex and evolves similarly to MCS1, except for a shorter length of the leading convective line. This MCS (MCS3) develops a stratiform region in the northeastern semicircle of AV (Fig. 5i), albeit a much less extensive one than in MCS1 because of the smaller spatial extent of FTR flows (cf. Figs. 5i and 5a). MCS3 evolves into a bow-shaped convective segment (Fig. 5j) with significant

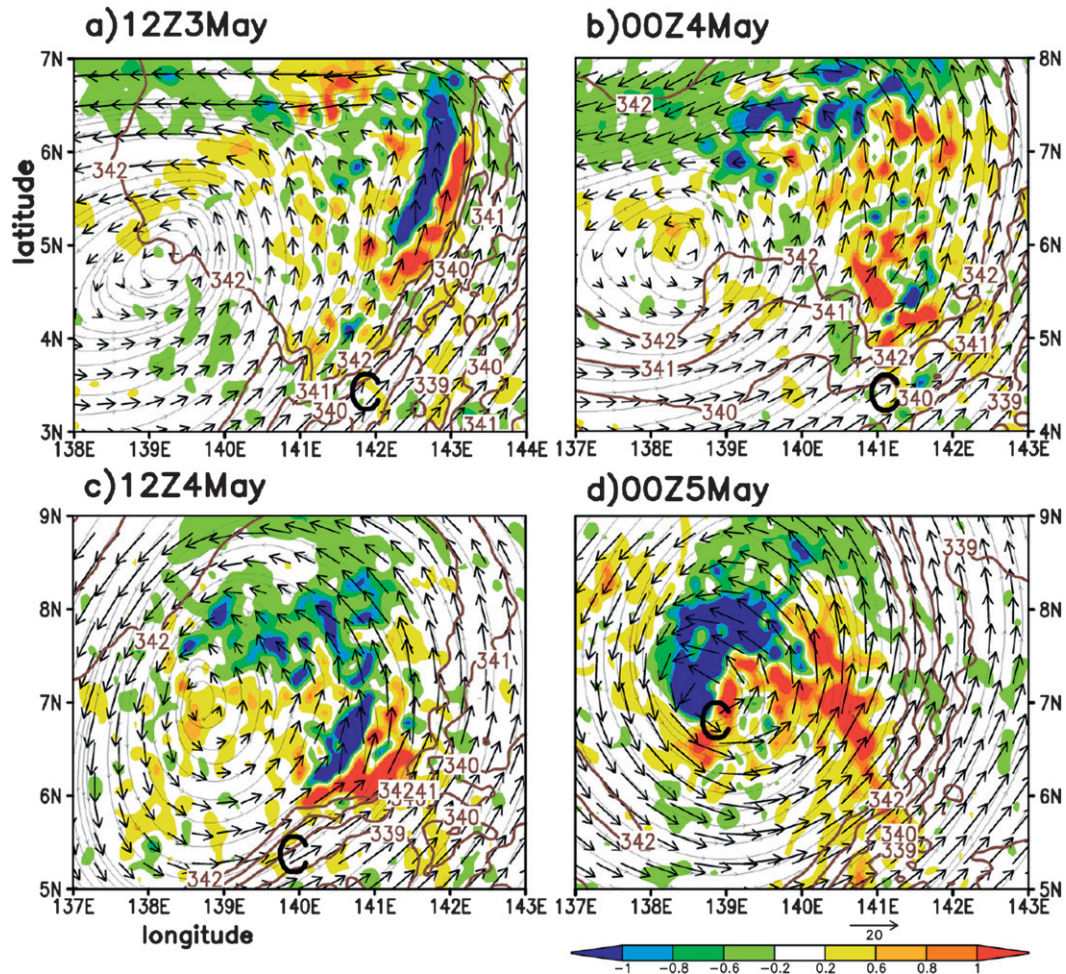


FIG. 8. As in Fig. 7, but for the horizontal divergence (shaded, $\times 10^{-4} \text{ s}^{-1}$) and θ_e (contoured at 1-K interval below 343 K), superposed with streamlines and flow vectors, at 600 hPa. All fields are taken as ± 3 -h averages at (a) 3/12–156, (b) 4/00–168, (c) 4/12–180, and (d) 5/00–192.

midlevel convergence behind the leading line and within the stratiform region (Fig. 8c). Associated with the bow-shaped convective region is the development of westerly RTF flow and easterly FTR ascending flow with intense cyclonic vorticity along the leading line, all of which resemble to a certain degree those associated with MCS1 (cf. Figs. 6a and 6c). The magnitude of midlevel cyclonic vorticity along the leading line of MCS3 is significantly greater than that in MCS1, likely associated with its close proximity to AV, which intensified due to the absorption of MCV V (see Fig. 2b).

However, even though the RTF flow at 4/12–180 is more extensive than that of MCS1 at 3/08–152, only a trough appears to the east of AV (Fig. 5j). Apparently, a well-developed MCV fails to develop in MCS3 because of the reduced vertical tilt of the WWB vortex. That is, the horizontal distance between the midlevel

and 900-hPa vortex centers (i.e., AV and C) has decreased from about 450 km at 3/00–144 to 200 km by 4/16–184. As a result, the arc-shaped rainband to the northeast of C is displaced northward to intersect with the southern part of MCS3 (cf. Figs. 5i and 5j), quickly eliminating the bow-shaped portion of the leading line (cf. Figs. 5j and 5k).

As the vertical tilt of the WWB vortex centers is further reduced, the remnants of MCS3 populate the center of midlevel vortex AV (Figs. 5j–l). This is an important transition, as it represents the transition from a divergent (Figs. 8a–c) to a convergent midlevel circulation center (Fig. 8d), in which ambient vorticity is stretched. It is well known that latent heat release close to the vortex center is very effective in deepening the surface cyclone (Hack and Schubert 1986), and presumably in intensifying the midlevel circulation as well.

e. MCS4: A spiral rainband

During the period from 4/16–184 to 5/00–192, the remnants of MCS3 (associated with AV) merge with the arc-shaped shallow rainband (associated with C) to form a comma-shaped one with stratiform clouds in the outer region (Fig. 5l). The leading line convection develops on the concave inward side of the arc because of the interaction of the enhanced midlevel flow with the low-level southeasterly inflow (cf. Figs. 5k,l and 7c). The concave structure of an MCS leading line is not often observed apart from the TC environment. While SI begins at 5/00–192 after the WWB vortex becomes upright, its larger-scale rotational flows still remain highly asymmetric, especially in the low levels (Figs. 5m and 7d). For example, the 900-hPa circulation remains meridionally elongated with convectively distorted flows to the north of C (see Figs. 7d and 5p), whereas the midlevel circulation AV becomes increasingly symmetric with time because of the continued absorption of CGVs (see Figs. 1 and 5) and strong convergence at its center (Fig. 8d). These flow structures are associated with the formation of the well-developed spiral rainband, defined as MCS4, roughly along the low-level streamlines (Figs. 5n–p). Axisymmetrization appears in the midlevel, as revealed by increasingly concentric streamlines, but not in the low-level diffluent regions where few convective cells could be triggered. Convective precipitation associated with MCS4 (i.e., the incipient primary rainband of Chanchu) is best described at this stage as occurring on the downshear left (Frank and Ritchie 1999; Black et al. 2002)—that is, to the north of the west-southwesterly VWS vector (Fig. 2b). The convective-scale interaction between MCS4 and the local vertical shear will be more closely examined in the third part of this series.

Unlike MCS1–MCS3, MCS4 does not exhibit significant moist downdrafts (cf. Figs. 7a–d), which is attributable to the continued moistening of atmospheric columns in the inner-core region and increased separation from the midlevel low- θ_e intrusion that generated cool downdrafts in previous MCSs (Fig. 8d). A vertical cross section along the spiral rainband in the inner-core region (Fig. 6d) shows prevailing cyclonically slantwise upward motion that is peaked at the midlevel as a result of the convective mixing of moist entropy and the convectively generated cyclonic vorticity in the inner-core region of MCS4, as typically seen in the eyewall of a hurricane (Liu et al. 1997). In this sense, MCS4 is quite unique compared to MCS1–MCS3. In fact, the four MCSs all have different characteristics in terms of orientation and shape, generation of MCVs and moist downdrafts, and dynamical lifting mechanisms (e.g., downtilt-right versus downshear-left, and cold pool).

Although more case studies are needed, the different MCSs may be typical of the convective evolution leading to TCG from a large-scale tilted vortex.

f. Convective contribution to the system-scale cyclonic vorticity

To help reveal the net contribution of the MCSs, let us first take a look at the tilted WWB vortex structures prior to 3/00–144 from the DRY run. Without the diabatic heating, the WWB vortex exhibits a more symmetric shape but much less vertical tilt than CTL (cf. Figs. 9a,b and 3b,c). The vertical tilt in DRY is also much less than that at the initial time, suggesting that the vortex resiliency (Reasor et al. 2004) plays an important role in vertically aligning the WWB vortex. The DRY circulation size is relatively smaller at 500 hPa and larger at 900 hPa than in CTL because of the lack of midlevel CGVs and low-level convergence with the WWB vortex, respectively. This helps explain the 5-hPa central pressure difference after the 144-h integration between the two runs (i.e., 1003 hPa in CTL versus 1008.5 hPa in DRY). Moreover, the WWB becomes shallower and less extensive in the absence of diabatic heating, as indicated by the easterly flow to the southeast of A (Fig. 9a). In particular, deep convection in CTL distorts substantially the vortex circulations to the north by generating an intense midlevel trough, which accounts for the general northward displacement (see the location of A_{dry} near the equator in Fig. 9a versus A near 4°N in Fig. 3b) via strong midlevel convergence there (Figs. 8a–c).

Figure 9c summarizes the vortical contributions of the four MCSs to the system-scale rotation at 12-h intervals. The mean vorticity profile in DRY at 3/00–144 is peaked near 850 hPa where the WWB is maximized, whereas the CTL profile is peaked near 500 hPa where the vorticity generation in the stratiform region is most pronounced (e.g., Figs. 6a–d). A comparison of the two profiles indicates that the diabatic heating, prior to 3/00–144, acts to enhance (suppress) midlevel (low-level) cyclonic vorticity at the system scale and to increase the depth of the WWB vortex circulation. Note though that while the low-level system-scale vorticity in CTL is weaker than that in DRY, likely because of the effects of cold downdrafts behind the leading convective lines, the local circulation of C and its minimum central pressure are still stronger as a result of larger-scale warming and general pressure falls associated with the MCSs. As the stratiform clouds decay after 3/00–144, the local peak vorticity near 500 hPa decreases slightly. However, continued convective development can account for the amplification of the system-scale cyclonic vorticity, which grows most rapidly between 900 and 600 hPa. The

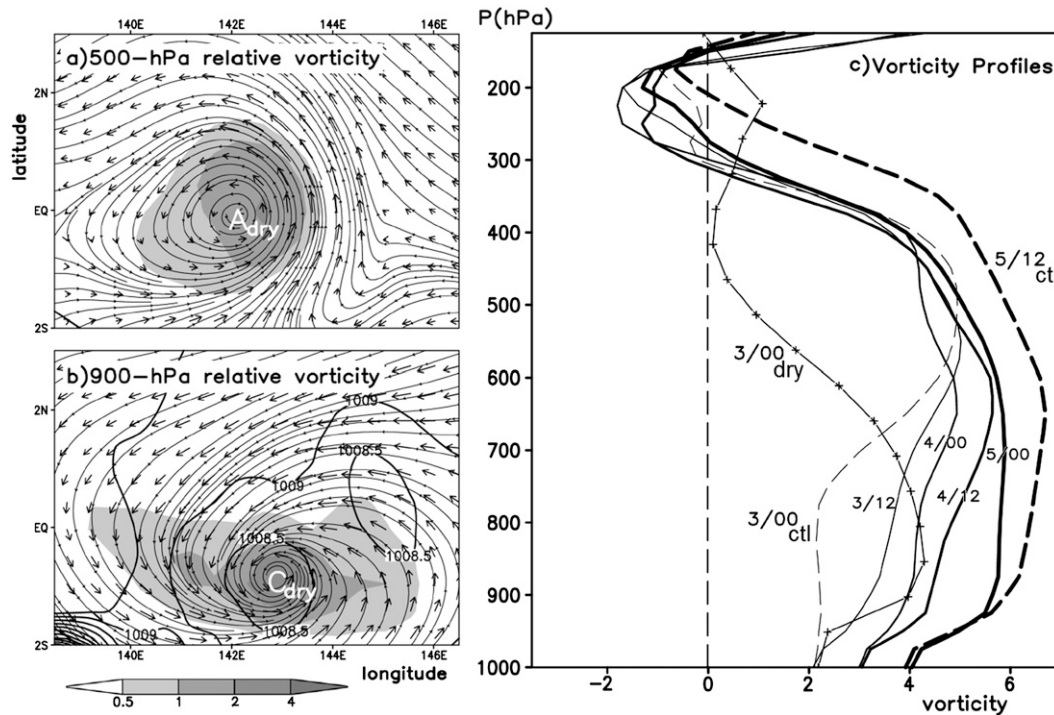


FIG. 9. Horizontal map of relative vorticity (shaded, 10^{-4} s^{-1}), streamlines, and flow vectors at (a) 500 and (b) 900 hPa from the 144-h dry run with the same size but centered farther south than in Figs. 3b,c. Solid lines in (b) denote the sea level pressure field. (c) Vertical profiles of the system-scale relative vorticity ($\times 10^{-5} \text{ s}^{-1}$) at 12-h intervals between 3/00–144 and 5/12–204. The 3/00 profile from the 144-h dry run is also given.

relatively small growth of the system-scale vorticity in the lowest 100-hPa layer, even after 5/00–192, could be attributed to the decreased vortex circulation size in the low levels, in addition to the MBL frictional effects. Although we reserve a detailed investigation of the vorticity generation mechanisms for Part III of this series of papers, it is sufficient to state from Fig. 9 that the contribution of the MCSs to the WWB vortex system is a net increase of the system-scale cyclonic vorticity in a deep layer of the troposphere.

4. Thermodynamic transition

We have shown above the transformation of the tilted WWB vortex to an upright one leading to SI beginning at 5/00–192. In this section we show why the surface pressure begins to fall continuously at this time. Davis and Bosart (2004) referred to the thermodynamic transformation of such a baroclinic disturbance to a warm-core TC as tropical transition, in contrast with extratropical transition from a TC to an extratropical disturbance. Obviously, it is mostly the CGVs of different scales that are responsible for such a tropical transition, based on the results presented above. However, it remains unclear how such a thermodynamic transformation occurs as a baroclinic

vortex transitions to a warm-core TC. For this purpose, Fig. 10 shows the vertical cross sectional evolution of the relative vorticity, cross-plane winds, and thermal anomalies of the WWB vortex up to the early SI stage. Note that the immediate influences of the MCSs are not included in the cross sections, since they occur on the downtilt-right side of the WWB vortex where favorable upward motion and latent heating are present (see Fig. 5).

It is evident that the WWB vortex decreases its vertical tilt (Figs. 10a–g) as the horizontal distance between A and C decreases from 450 to 200 km during the 24-h period of 3/12–156 and 4/12–180. However, the mid- and low-level vortex layers appear to evolve separately by different mechanisms. That is, A amplifies in both magnitude and depth at a location where little precipitation is present, so it must result from the absorption of the MCV and CGVs that are generated in the MCSs occurring on the downtilt-right side of the WWB vortex, as discussed in section 3. By comparison, C maintains a nearly constant magnitude, also shown in Fig. 2, but its depth remains below 700 hPa until 4/18–186 owing to the latent heat release along the arc-shaped shallow rainband nearby. On the other hand, significant upward motion begins above the center of AV in association with increasing midlevel convergence there after 4/18–186 (Fig. 8c). Thus, the tilted WWB vortex

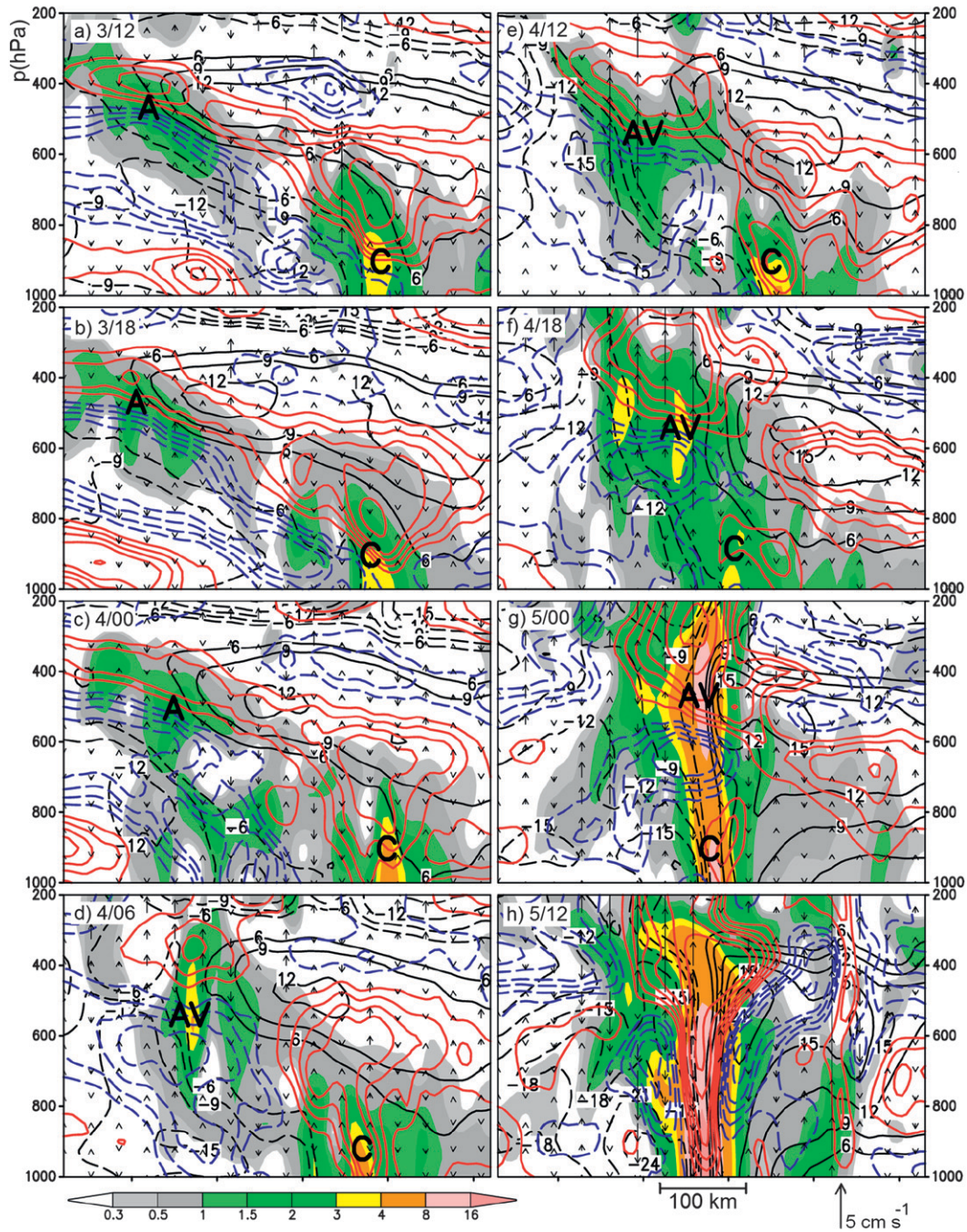


FIG. 10. Vertical cross sections of the relative vorticity (shaded, 10^{-4} s^{-1}) and cross-plane wind speed into (out of) the vertical plane [black solid (dashed) contours at 3 m s^{-1} interval], superimposed with deviation temperatures (colored contours at $\pm 0.2, 0.4, 0.6, 0.8, 1.2, 1.6,$ and 2.0°C), and vertical motion vectors. They are taken at (a) 3/12–156, (b) 3/18–162, (c) 4/00–168, (d) 4/06–174, (e) 4/12–180, (f) 4/18–186, (g) 5/00–192, and (h) 5/12–204 from the 6-km resolution domain. Each field has been laterally averaged $\pm 18 \text{ km}$ to show more representative features.

exhibits two peak cyclonic vorticity centers with large circulation asymmetries during genesis (see Figs. 10a–e). All of these differ from those observed in DRY, in which the positive relative vorticity is more uniformly tilted between 900 and 500 hPa (Figs. 9a,b).

The different behaviors of the mid- and low-level vortex layers also give rise to two different RMWs: one in the 600–400-hPa layer and the other in the 1000–800-hPa layer, and they persist even 12 h after the onset of SI, e.g., at 5/12–204 (see Figs. 4b and 10). Specifically, the mid-level peak tangential wind in the cross sections increases from 12 to 21 m s^{-1} with reduced asymmetries while its associated RMW decreases from near 500 km at 3/00–144 to 150 km at 4/18–186, and to about 50 km at 5/12–204, indicating the spin-up of the midlevel cyclonic circulation. In contrast, the low-level tangential winds increase slowly, e.g., from 12 to 15 m s^{-1} during this same period, but more rapidly to 24 m s^{-1} by 5/12–204; and they remain highly asymmetric even after the onset of SI. All these are consistent with the growth of the system-scale cyclonic vorticity shown in Figs. 2b and 8c, and the circulation structures shown in Fig. 5.

One can see from Fig. 10 that large VWS in tangential flow (e.g., $>24 \text{ m s}^{-1}$ between 900 and 400 hPa at 3/12–156) is always present across the tilted vortex layer, which is consistent with the thermal gradient across the layer with a tilted warm (cool) layer above (below). Moreover, the vertical thermal couplet associated with AV is gradually separated from the low-level counterpart as the midlevel vortex amplifies. At 4/18–186 (Fig. 10f), AV resembles to a certain degree a barotropic vortex with a warm column above a cold one (e.g., see Figs. 10d,e), just like a single MCV shown in Zhang and Bao (1996b, see Figs. 4 and 5 therein). Of interest is that AV's cold column gradually erodes into the low-level C's warm-core region as the horizontal distance between the two shrinks. This cold erosion coincides with the development of intense convection in the core region of AV, but with strong upward above weak downward motion (cf. Figs. 5m and 10g). In fact, the vertical motion field always exhibits more favorable upward motion in the vicinity of AV than that of C due to the distribution of convection in the northern semicircle, which is consistent with the vorticity growth and vortex contraction characteristics in the two vortex layers. This suggests that the cold layer below the tilted vortex tends to suppress upward motion.

We can see from Figs. 10f,g that the subsidence warming induced by diabatic heating in the inner-core region may play an important role in eliminating the cold anomaly. Then, the upper-level warm core becomes vertically aligned with the low-level one, causing a net increase of the warm-core depth (and intensity) above

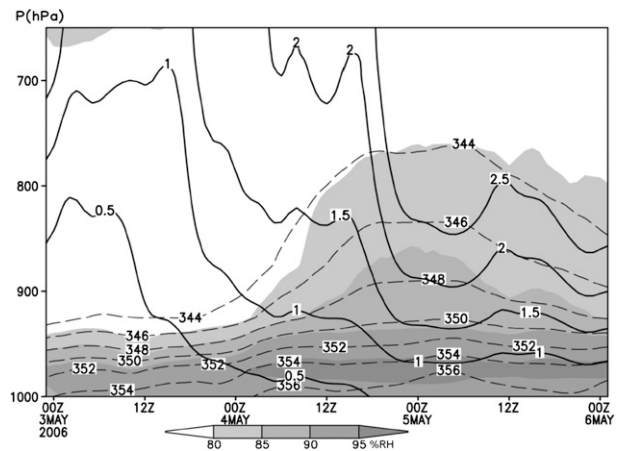


FIG. 11. Pressure–time cross section of the storm-scale RH (shaded, %) and θ_e (dashed contours at 2-K interval above 344 K), and vertical motion (thick solid contours at 0.5 cm s^{-1} interval) during the period between 3/00–144 and 6/00–216 from the 6-km resolution domain.

C. This thermodynamic transformation process would hydrostatically result in the surface pressure falls and the triggering of the wind-induced surface heat exchange (WISHE) processes (Emanuel 1987), as indicated by the increased surface winds, surface heat fluxes and pressure falls (see Figs. 2a and 10f–h). In this regard, the vortical contribution of deep convection to the midlevel system-scale cyclonic vorticity, as shown in Figs. 2b and 9, should be considered as the buildup of a balanced warm core (and the increased cyclonic rotation) that can cause hydrostatic pressure falls at the surface, especially when it is superimposed onto a low-level cyclonic circulation. Note that this thermodynamic transformation differs from that presented by Zhang and Bao (1996b), in which a surface-based cold dome underneath a midlevel MCV is transformed to a warm-core column as a result of the upward sensible heat fluxes from the underlying warm ocean, and horizontal advection by convectively generated circulations in a spiral rainband.

The trigger of the WISHE processes leading to SI has attracted some attention in the recent literature. Kieu and Zhang (2008) show the important role of a vortex merger in the rapid increase of surface heat fluxes and the trigger of SI leading to Tropical Storm Eugene (2005). From the simulation of an idealized mesovortex, Nolan (2007) finds that the key to SI is the convective moistening over a sufficient depth of the troposphere in the core region of the vortex, and a recent study by Camargo et al. (2009) also shows that the relative humidity (RH) is the most important contribution of the MJO to TCG. To examine to what extent Nolan's finding could be applied to the present case, the pressure–time cross sections of several area-averaged quantities centered at C during a 3-day

period encompassing the pregenesis and genesis stages are given in Fig. 11, which shows that RH and θ_e remain nearly constant prior to 4/00–168, with RH < 80% above 900 hPa. Subsequently, both quantities increase. That is, the system-scale RH of 85% (80%) extends to 850 (750) hPa after the life cycles of MCS1–MCS3, and then remains nearly steady during the life cycle of MCS4. Such high RH is considered by Nolan (2007) and others as one of the preconditions for TCG, but the SI of Chanchu and rapid increase in surface fluxes and surface θ_e value in the present case do not occur until the vortex becomes upright during the life cycle of MCS4. This implies that a deep-layered humidification of the troposphere may be a necessary but not sufficient condition for SI. Given the moist environment, we may state that the formation of an upright vortex in the present case is the sufficient condition for the trigger of SI. The establishment of a deep warm column allows the sustained fall of central pressure, leading to the positive feedback between the sea surface winds, heat fluxes, and latent heat release, i.e., the trigger of the WISHE process (see Fig. 2). This mechanism may account for the tropical transition of many Atlantic TCs that have a baroclinic origin (Davis and Bosart 2004).

5. Summary and conclusions

In this study, we examined the life cycles of a series of four major MCSs and the resulting thermodynamic transformation of a tilted WWB vortex to the warm-core Typhoon Chanchu (2006) near the equator. This was achieved through analysis of an 11-day cloud-resolving simulation of the case presented in Part I of this series of papers. The tilted WWB vortex is shown to exhibit an elevated cold-core layer below and a weak warm column above with large VWS across the vortex layer at earlier stages, and a surface-based warm-core circulation in the lowest 300 hPa layer; the midlevel and surface-based warm cores are separated by more than 450 km 2 days prior to SI.

Figure 12 depicts schematically how the four MCSs, which are favored on the downtilt-right side of the WWB vortex (see Part I for more details), change shape depending on the vertical tilt of the vortex relative to the larger-scale easterly flows. The MCSs develop initially as a squall line with trailing stratiform precipitation and an incipient MCV at the northern end of the convective line (Fig. 12a; MCS1), when the WWB vortex is westward-tilted. They evolve to a mesoscale convective cluster whose shape changes from an inverted U to a question mark (Fig. 12b; MCS2) as the MCV matures and merges with the midlevel portion of the tilted WWB vortex. Then the leading convective line is cut off by an intensifying arc-shaped shallow rainband from the south as the lower-level

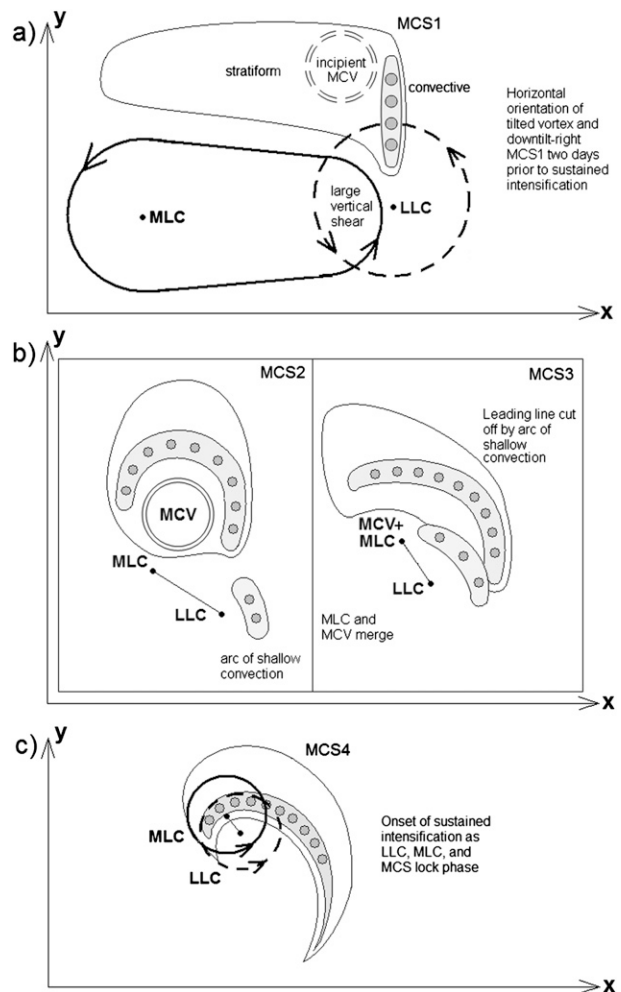


FIG. 12. Schematic depiction of (a) the horizontal distribution of the tilted WWB vortex and the downtilt-right MCSs, (b) the interaction of the MCSs with the tilted vortex leading to a near-upright orientation, and (c) the horizontal distribution of the vortex near the onset of SI. MLC and LLC indicate the locations of the midlevel (600 hPa) and lower-level (900 hPa) vortex centers, respectively.

cyclonic circulation slowly increases (Figs. 12b and 2a; MCS3). The first spiral rainband forms as the WWB vortex decreases its vertical tilt (Fig. 12c; MCS4). The arc-shaped shallow rainband likely helps to maintain the surface-based vortex. The model reproduces the downshear-left generation of precipitation associated with an upright TC vortex near the onset of SI. Results show that strong cold pools tend to be favored behind the leading convective lines during the earlier tilted-vortex stages due primarily to dry intrusion by the midlevel sheared flows, but few cold pools develop when the WWB vortex becomes more upright and sufficiently moist at the later stages.

It is found that the upper-level warm column increases in depth and intensity as a result of absorbing CGVs, including an MCV, by the WWB vortex. In particular, the

midlevel circulation of the WWB vortex intensifies with size contraction during genesis. By comparison, despite the continued convective development during genesis, the surface-based vortex persists with little deepening for more than 2 days due partly to the presence of descending motion and lower- θ_e air on the downtilt left side of the WWB vortex and partly to the presence of large VWS, both acting to produce the arc-shaped shallow rainband in its vicinity that is not as efficient as wrap-around deep convection in TCG. Despite the convective moistening of the lower troposphere, the SI of Chanchu is not triggered until the WWB vortex aligns in the vertical. That is, the superposition of the surface-based and elevated warm cores marks the thermodynamic transformation to a deep warm-core TC, leading to continuous hydrostatic pressure falls and the trigger of the WISHE process. This vertical alignment process, in which preexisting low- and midlevel portions of a tilted vortex are superimposed, differs from the so-called top-down and bottom-up processes discussed in previous studies that propose vertical extension of a vortex.

We may state that the contributions of the MCSs during the genesis stage of Chanchu include a) the generation of cyclonic vorticity and its storage, mostly in the midtroposphere, after merging CGVs within the WWB vortex; b) the convective moistening of the low- and midtroposphere; c) the forced (northward) displacement of the WWB vortex; and d) the reduced vertical tilt of the WWB vortex.

In Part III of this series of papers, we will continue to examine the impact of convective processes on the amplification of the midlevel circulations during the genesis and early SI stages, but at the convective scale using the 2-km resolution model results, and attempt to understand the dynamic mechanisms, including critical interactions between convection and vertical shear, whereby the *surface* circulation is amplified after the WWB vortex becomes vertically upright.

Acknowledgments. We thank Dr. Chanh Q. Kieu for invaluable discussions leading to the current study, as well as two anonymous reviewers whose detailed and thoughtful comments significantly improved the manuscript. This work was supported by ONR Grant N000140710186, and NSF ATM0758609.

REFERENCES

- Bartels, D. L., and R. A. Maddox, 1991: Midlevel cyclonic vortices generated by mesoscale convective systems. *Mon. Wea. Rev.*, **119**, 104–118.
- Biggerstaff, M. I., and R. A. Houze Jr., 1991: Kinematic and precipitation structure of the 10–11 June 1985 squall line. *Mon. Wea. Rev.*, **119**, 3034–3065.
- Bister, M., and K. A. Emanuel, 1997: The genesis of Hurricane Guillermo: TEXMEX analyses and a modeling study. *Mon. Wea. Rev.*, **125**, 2662–2682.
- Black, M. L., J. F. Gamache, F. D. Marks, C. E. Samsury, and H. E. Willoughby, 2002: Eastern Pacific Hurricanes Jimena of 1991 and Olivia of 1994: The effect of vertical shear on structure and intensity. *Mon. Wea. Rev.*, **130**, 2291–2312.
- Bracken, W. E., and L. F. Bosart, 2000: The role of synoptic-scale flow during tropical cyclogenesis over the North Atlantic Ocean. *Mon. Wea. Rev.*, **128**, 353–376.
- Braun, S. A., M. T. Montgomery, K. J. Mallen, and P. D. Reasor, 2010: Simulation and interpretation of the genesis of Tropical Storm Gert (2005) as part of the NASA Tropical Cloud Systems and Processes Experiment. *J. Atmos. Sci.*, **67**, 999–1025.
- Camargo, S. J., M. C. Wheeler, and A. H. Sobel, 2009: Diagnosis of the MJO modulation of tropical cyclogenesis using an empirical index. *J. Atmos. Sci.*, **66**, 3061–3074.
- Davis, C. A., and F. Bosart, 2003: Baroclinically induced tropical cyclogenesis. *Mon. Wea. Rev.*, **131**, 2730–2747.
- , and —, 2004: The TT problem: Forecasting the tropical transition of cyclones. *Bull. Amer. Meteor. Soc.*, **85**, 1657–1662.
- Emanuel, K. A., 1987: An air–sea interaction model of intraseasonal oscillations in the tropics. *J. Atmos. Sci.*, **44**, 2324–2340.
- Frank, W. M., and E. A. Ritchie, 1999: Effects of environmental flow upon tropical cyclone structure. *Mon. Wea. Rev.*, **127**, 2044–2061.
- Fritsch, J. M., J. D. Murphy, and J. S. Kain, 1994: Warm core vortex amplification over land. *J. Atmos. Sci.*, **51**, 1780–1807.
- Gamache, J. F., and R. A. Houze, 1982: Mesoscale air motions associated with a tropical squall line. *Mon. Wea. Rev.*, **110**, 118–135.
- Gray, W. M., 1998: The formation of tropical cyclones. *Meteor. Atmos. Phys.*, **67**, 37–69.
- Hack, J. J., and W. H. Schubert, 1986: Nonlinear response of atmospheric vortices to heating by organized cumulus convection. *J. Atmos. Sci.*, **43**, 1559–1573.
- Harr, P. A., and R. L. Elsberry, 1996: Structure of a mesoscale convective system embedded in Typhoon Robyn during TCM-93. *Mon. Wea. Rev.*, **124**, 634–652.
- , M. S. Kalafsky, and R. L. Elsberry, 1996: Environmental conditions prior to formation of a midlevel tropical cyclone during TCM-93. *Mon. Wea. Rev.*, **124**, 1693–1710.
- Hendricks, E. A., M. T. Montgomery, and C. A. Davis, 2004: The role of “vortical” hot towers in the formation of Tropical Cyclone Diana (1984). *J. Atmos. Sci.*, **61**, 1209–1232.
- Hogsett, W., and D.-L. Zhang, 2010: Genesis of Typhoon Chanchu (2006) from a westerly wind burst associated with the MJO. Part I: Synoptic evolution of a vertically tilted vortex. *J. Atmos. Sci.*, **67**, 3774–3792.
- Houze, R. A., Jr., 2004: Mesoscale convective systems. *Rev. Geophys.*, **42**, RG4003, doi:10.1029/2004RG000150.
- , S. A. Rutledge, M. I. Biggerstaff, and B. F. Smull, 1989: Interpretation of Doppler weather radar displays of midlatitude mesoscale convective systems. *Bull. Amer. Meteor. Soc.*, **70**, 608–619.
- Kieu, C. Q., and D.-L. Zhang, 2008: Genesis of Tropical Storm Eugene (2005) from merging vortices associated with the ITCZ breakdowns. Part I: Observational and modeling analyses. *J. Atmos. Sci.*, **65**, 3419–3433.
- Liu, Y., D.-L. Zhang, and M. K. Yau, 1997: A multiscale numerical study of Hurricane Andrew (1992). Part I: Explicit simulation and verification. *Mon. Wea. Rev.*, **125**, 3073–3093.

- Menard, R. D., and J. M. Fritsch, 1989: A mesoscale convective complex-generated inertially stable warm core vortex. *Mon. Wea. Rev.*, **117**, 1237–1261.
- Montgomery, M. T., M. E. Nicholls, T. A. Cram, and A. B. Saunders, 2006: A vortical hot tower route to tropical cyclogenesis. *J. Atmos. Sci.*, **63**, 355–386.
- Nolan, D. S., 2007: What is the trigger for tropical cyclogenesis? *Aust. Meteor. Mag.*, **56**, 241–266.
- Reasor, P. D., M. T. Montgomery, and L. D. Grasso, 2004: A new look at the problem of tropical cyclones in vertical shear flow: Vortex resiliency. *J. Atmos. Sci.*, **61**, 3–22.
- Ritchie, E. A., and G. J. Holland, 1997: Scale interactions during the formation of Typhoon Irving. *Mon. Wea. Rev.*, **125**, 1377–1396.
- , and —, 1999: Large-scale patterns associated with tropical cyclogenesis in the western Pacific. *Mon. Wea. Rev.*, **127**, 2027–2043.
- Simpson, J., E. Ritchie, G. J. Holland, J. Halverson, and S. Stewart, 1997: Mesoscale interactions in tropical cyclone genesis. *Mon. Wea. Rev.*, **125**, 2643–2661.
- Weisman, M. L., and C. A. Davis, 1998: Mechanisms for the generation of mesoscale vortices within quasi-linear convective systems. *J. Atmos. Sci.*, **55**, 2603–2622.
- Yuter, S. E., and R. A. Houze Jr., 1998: The natural variability of precipitating clouds over the western Pacific warm pool. *Quart. J. Roy. Meteor. Soc.*, **124**, 53–99.
- Zhang, D.-L., 1992: The formation of a cooling-induced mesovortex in the trailing stratiform region of a midlatitude squall line. *Mon. Wea. Rev.*, **120**, 2763–2785.
- , and J. M. Fritsch, 1987: Numerical simulation of the meso- β scale structure and evolution of the 1977 Johnstown flood. Part II: Inertially stable warm-core vortex and the mesoscale convective complex. *J. Atmos. Sci.*, **44**, 2593–2612.
- , and N. Bao, 1996a: Oceanic cyclogenesis as induced by a mesoscale convective system moving offshore. Part I: A 90-h real-data simulation. *Mon. Wea. Rev.*, **124**, 1449–1469.
- , and —, 1996b: Oceanic cyclogenesis as induced by a mesoscale convective system moving offshore. Part II: Genesis and thermodynamic transformation. *Mon. Wea. Rev.*, **124**, 2206–2225.
- , K. Gao, and D. B. Parsons, 1989: Numerical simulation of an intense squall line during 10–11 June 1985 PRE-STORM. Part I: Model verification. *Mon. Wea. Rev.*, **117**, 960–994.
- Zipser, E. J., and C. Gautier, 1978: Mesoscale events within a GATE tropical depression. *Mon. Wea. Rev.*, **106**, 789–805.